



UNIVERSITY OF LEEDS

This is a repository copy of *Micro-mechanical properties of single high aspect ratio crystals*.

White Rose Research Online URL for this paper:  
<http://eprints.whiterose.ac.uk/149357/>

Version: Accepted Version

---

**Article:**

Hallac, FS [orcid.org/0000-0001-6121-0608](https://orcid.org/0000-0001-6121-0608), Fragkopoulos, IS, Connell, SD et al. (1 more author) (2019) Micro-mechanical properties of single high aspect ratio crystals. CrystEngComm, 38. pp. 5738-5748. ISSN 1466-8033

<https://doi.org/10.1039/C9CE00819E>

---

© The Royal Society of Chemistry 2019. This is an author produced version of a paper published in CrystEngComm. Uploaded in accordance with the publisher's self-archiving policy.

**Reuse**

Items deposited in White Rose Research Online are protected by copyright, with all rights reserved unless indicated otherwise. They may be downloaded and/or printed for private study, or other acts as permitted by national copyright laws. The publisher or other rights holders may allow further reproduction and re-use of the full text version. This is indicated by the licence information on the White Rose Research Online record for the item.

**Takedown**

If you consider content in White Rose Research Online to be in breach of UK law, please notify us by emailing [eprints@whiterose.ac.uk](mailto:eprints@whiterose.ac.uk) including the URL of the record and the reason for the withdrawal request.



[eprints@whiterose.ac.uk](mailto:eprints@whiterose.ac.uk)  
<https://eprints.whiterose.ac.uk/>

# Micro-mechanical properties of single high aspect ratio crystals

François S. Hallac<sup>a</sup>, Ioannis S. Fragkopoulos<sup>a</sup>, Simon D. Connell<sup>b</sup>, Frans L. Muller<sup>a,\*</sup>

<sup>a</sup> School of Chemical and Process Engineering, University of Leeds, Leeds, LS2 9JT, UK.

<sup>b</sup> School of Physics and Astronomy, University of Leeds, Leeds, LS2 9JT, UK.

## Abstract

This work describes a new method to measure breakage strength and elastic modulus of single crystal cantilevers using atomic force microscopy. Crystal breakage is an important but poorly understood factor in mechanical processing of organic crystals. In this study, 300 $\mu\text{m}$  long beta glutamic acid, needle-shaped crystal cantilevers are bend and broken in an Atomic Force Microscope. We report the first directly measured distribution of breakage strength and Young's modulus of an organic crystal material. The distribution follows a Weibull distribution; 50% of the crystals break at less than 22.4MPa and have a Young's modulus below 1.90GPa and we observed that stronger crystals are stiffer, and thicker crystals break easier. The data generated from the single crystal cantilever method provides fundamental material properties essential for understanding undesirable crystal fracture due to forces exerted on crystals in manufacturing processes such as crystallisation, filtration and drying.

**Keywords:** Breakage Strength, Young's modulus, organic crystals, mechanical properties, Atomic Force Microscopy.

# 1. Introduction

The majority of pharmaceutical and fine chemical active ingredients consist of high aspect ratio particles such as needles and plates. Such highly elongated materials are significantly prone to undesired breakage during manufacturing processes such as filtration [1] and drying [1, 2] where crystals are subjected to significant forces by the processing equipment. Changes in particle size distribution can significantly affect downstream processing characteristics of active pharmaceutical ingredients (APIs) [3], and can unintentionally alter critical quality attributes, affecting patients [4]. For instance, in an agitated pressure filter dryer high aspect ratio crystals form an open structure in which crystals are deposited on top of each other. In such structure forces, applied by pressurising the equipment or rotation of the agitator, are conveyed via the contact points between two crystals touching each other. High aspect ratio particles have multiple contact points along their long axis which leads to crystal bending. Undesired breakage occurs when the incurred bending stress is higher than the critical strength of a crystal [5].

The fundamental mechanical properties data to underpin a mechanistic postulate such as the one described above is largely missing for organic crystalline materials. Yet, mechanical properties such as Young's modulus  $E$ , tensile strength  $\sigma_c$  and the critical stress factor  $K_{Ic}$  are fundamental to linking the impact of forces at macro or process scale to the behaviour of crystals at the micro scale. This is highly relevant for processes such as crystallisation, filtration, drying, granulation, milling and compaction as crystals are exposed to significant force.

Organic crystals are usually formed by solvent crystallisation as small crystals, typically with high aspect ratios (e.g. needles, plates). As these materials are not

typically used for construction, measurement data has lagged behind compared to inorganic materials and polymers.

Roberts et al. [6, 7] formed macroscopic square bars with varying porosity and, by extrapolating to zero porosity, determined mechanical properties of organic materials, summarised in table A II. The observed breakage strengths varied between  $\sigma_B = 4$  to 25 MPa and the Young's modulus between 3 and 24 GPa. They also measured the critical stress index, an important measure to describe the shattering of crystals under high impact [8], and reported  $K_{IC} = 0.1$  to  $0.35 \text{ MPa m}^{\frac{1}{2}}$ . Under the assumption that the surface energy is significantly less than the energy required to plastically deform the material near the tip of a crack ( $J_{IC}$ , the toughness), the breakage strength  $\sigma_C$  and  $K_{IC}$  are correlated by:

$$\sigma_B = \frac{K_{IC}}{\sqrt{\lambda}} = \sqrt{\frac{E J_{IC}}{\lambda}} \quad (1)$$

Where  $\lambda$  is the average flaw length (or crack length). Table A.II gives the crack lengths for the materials they studied, interestingly, the crack lengths are similar to typical width and/or thickness of crystals found after crystallisation (5 – 400 $\mu\text{m}$ ).

Ast et al [9] reviewed the experimental approaches to measure fracture toughness and identifies three key methods: (i) Nano indentation, (ii) micro pillar splitting (not discussed in this paper) and (iii) micro cantilever testing. Nano-indentation is widely used to assess mechanical properties, typically KIC, E, and hardness. Nano indentation assesses these properties on, and close to, the surface of the solid. An indenter, the apex of a small pyramidal shape, is used to penetrate the crystalline material leading to the formation and propagation of cracks. The observed crack length and propagation can consequently be employed to determine the fracture toughness

$K_{IC}$ , and Young's modulus  $E$ , but not the breakage strength of APIs. Very detailed work on Sucrose [10] shows that the elasticity is dependent on the phase of the crystal investigated as may be expected from crystallographic considerations. This method gives similar values for the Young's modulus of organic molecules [11] to those obtained by extrapolation of porosity and excipients (Table A II). The values of the critical stress index are however an order of magnitude lower when measured by nano indentation compared to porosity extrapolation. Nano-indentation experiments have also been performed using the tip of the Atomic Force Microscope's cantilever (AFM) [12]. Relevant results are  $E \approx 2.5$  GPa for polymer films [13] and the hardness of a number of organic materials [14].

The micro cantilever method require the construction of the pillar/beam using lithographic or micro machining methods. In 2000 Namazu et al described a three point bending tests using AFM to determine tensile (breaking) strength and elastic modulus of Si [15]. This work showed a both elasticity and breakage strength could be measured for well-defined lithographically engineered silicon structures. The elasticity was reproducible, and the bending stress followed

Nano-indentation systems have also been used to conduct of 3-point bending experiments of Schiff bases [16]. These materials have a very low Young's modulus, ( $E = 0.190 - 0.880$  GPa) which was attributed to the presence of weak hydrogen-logen and halogen-halogen interactions which are easily broken and reformed, thus allowing the molecules to easily slip over each other. Plastic deformation is however prevented by interlocking of crystallographic planes so as to hinder long range molecular movement.

In this study, we present an alternative single crystal cantilever method to measure micro-mechanical properties of single organic materials, which are often unstable at

their melting point, making it difficult to prepare the homogeneous large scale samples used in mechanical property testing (e.g. beams, dumbbells), nor are they easily manipulated using lithographic methods commonly used on inorganic substances.

## **2. Materials & Methods**

### **2.1. Organic crystals**

The needle-shaped beta polymorph of glutamic acid was the selected organic material. A 99% purity glutamic acid powder provided by Sigma-Aldrich was recrystallised [17]. The glutamic acid powder was dissolved in deionised water and heated up to 70°C. The solution was cooled down to 60°C and previously crushed  $\beta$ -LGA seed material was added to the solution. The solution was held for 2 hours and then slowly cooled down to 20°C at approximately 3.5 °C/h allowing the crystals time to grow. The  $\beta$ -LGA crystals produced have of a length in the order of 0.1 to 1 mm. (Figure 1)

### **2.2. Metallic support**

A 303 stainless steel metallic piece of 5x5x2mm, small enough to fit in the AFM stub, was milled using a DMG 40evo machine with a milling cutter of 0.8 mm diameter to give three corridors (1mm width each and with 0.5mm distance between each other) in both sides of the piece (Figure 2a). This design allows the measurement of three crystals per face - 6 crystals in total (as in Figure 2b). The rectangular corners of the corridors ensured about 90° (+/-10%) angle between the crystal (cantilever) and the steel support. The steel's hardness guarantees that the crystals' breakage strength is

not affected by movement of the support. The height and width of the crystals can be observed with lateral and top down microscopy.

### **2.3. Sample preparation**

Industrial superglue (Everbuild products industrial super glue gp CYN50) composed of ethyl-2-cyanoacrylate was mixed with acetone in a 1:5 (glue:acetone) volume ratio, providing sufficient bonding strength and not affecting the physical and chemical properties of the  $\beta$ -LGA crystals [18, 19]. The designed metallic piece was glued on the AFM magnetic stub in such a way so that the corner with the highest corridor height was placed at the centre of the stub (see Figure 2). Beta-LGA crystals were carefully dropped on the metallic piece to minimise potential fragmentation. The higher elongated and better-shaped crystals were manoeuvred with fine tweezers within each corridor towards its edge as cantilevers. About 1  $\mu$ L glue mixture was dispersed on each corridor using an Acura 825 micro-dispenser with 0.1–10  $\mu$ L micropipette tip. The glue spreading was carefully controlled to avoid any movement of the crystals due to capillary flow, and to prevent the spreading of the glue past the metallic support edge and the subsequent coating of the cantilever part of the crystal.

After each breakage experiment, the metallic piece was washed in an acetone bath followed by a 30 min ultrasonic bath wash (James SONIC 3MX) to remove the glue mixture and the crystals

### **2.4. Cantilever sizing & AFM**

The macro-system light microscope (Motic SMZ-168) with a built-in AxioCam camera (ERc5s) was used for the observation of the crystals. The cantilevers' dimensions

(length, width and height) were measured using the AxioVision 7 software (as in Figure 3). The crystals were considered as cuboids.

A Bruker Multimode 8 atomic force microscope using the stiffest Bruker RTESP-525 AFM probe model was used to enable apply force onto the organic beta-LGA crystal cantilever. A Bruker Sapphire-12M sample was used for the AFM probe calibration; the deflection error sensitivity of the laser sensors was estimated to be equal to 45 nm/V (+/-50%) using the gradient of a ramp curve (small deflection) on the sapphire's hard surface (as in Figure 4) [20]. The probe's spring constant  $k_p$  was taken to be the manufacturer's value of  $k_p = 200 \text{ N/m}$ .

## 2.5. Force measurement

With the prepared stub in the AFM, the AFM probe was engaged at the edge of the crystal cantilever (as in Figure 5a). A ramp curve was performed on the cantilever's edge (see Figure 5b) to determine the system (probe & crystal) spring,  $k_T$ ; the system spring was equal to the gradient of the loading curve (see Figure 6). The AFM step motor was then used to apply a load at the crystal's edge by lowering the AFM probe step-by-step in a quasi-static way until crystal breakage was occurred (cf. Figure 7). No significant indentation of the AFM tip into the glutamic acid crystal has been observed, and it is therefore assumed the error due to deformation at the AFM tip is negligible.

Beta-LGA was considered here as linear-elastic material (based on the elastic nature of similar organic materials [16]) and consequently, the  $\beta$ -LGA crystal cantilever was considered to have a linear spring. The applied force was obtained using Hooke's law [21]:

$$F = k_C \cdot \delta_C \quad (2)$$

where  $F$  is the applied force [N],  $k_C$  the crystal spring [N/m] and  $\delta_C$  the deflection of the crystal [m]. The crystal spring was calculated by (see derivation in Appendix A.1):

$$k_C = \frac{k_P \cdot k_T}{k_P - k_T} \quad (3)$$

here  $k_T$  is the system spring [N/m] and  $k_P$  the probe's spring constant. The deflection of the crystal,  $\delta_C$ , was expressed as (see derivation in Appendix A.2):

$$\delta_C = \delta_T \cdot \frac{k_P}{k_P + k_C} \quad (4)$$

With  $\delta_T$  is the step motor deflection [m] given by:

$$\delta_T = n_{steps} \cdot S_m \quad (5)$$

$n_{steps}$  is the number of the step motor steps and  $S_m$  is the deflection per step. The deflection for 9 motor steps was measured to be 4.2  $\mu\text{m}$  making  $S_m = 0.466 \mu\text{m}/\text{step}$ .

## 2.6. Broken crystal part measurement

The beta-LGA organic crystals were not identical and the position at which crystal breakage was occurred was different for each crystal. The length of each crystal's broken part,  $L_B$ , was calculated by (cf. Figure 8a):

$$L_B = L - L_A \quad (6)$$

where  $L$  is the total crystal cantilever length [m] and  $L_A$  the length of the crystal's remaining part [m], which was measured using the light microscope after each breakage event (see Figure 8b).

## 2.7. Breakage strength & Young's modulus

Having the individual beta-LGA crystal dimensions at hand, one can calculate the Young's modulus,  $E$ , using [22]:

$$E = \frac{4 k_c L^3}{w h^3} \quad (7)$$

$w$  is the crystal's width [m] and  $h$  the crystal's height [m]. Note that  $E$  is based on forces applied by the AFM directly and  $k_c$  results from the measured force ramp (Figure 6, and eq 3).

The breakage strength,  $\sigma_B$ , was estimated using a derivative from the Euler-Bernoulli beam theory [1, 23]. For a rectangular beam:

$$\sigma_B = F_B \frac{6 L_B}{w h^2} = \frac{n_{steps} S_m k_p}{\left(1 + \frac{k_T}{k_P - k_T}\right) \left(\frac{k_P}{k_T} - 1\right)} \frac{6 L_B}{w h^2} \quad (8)$$

where  $F_B$  is the applied force that leads to crystal breakage [N]. The breakage force was calculated using equations (2) to (5) and the total number of motor steps that led to crystal breakage. The length of each crystal's broken part,  $L_B$ , was used here to calculate the stress on the breakage site of the crystal.

## 2.8. Beam bending simulations

The linear elastic material solid mechanics model, available in COMSOL structural mechanics suite, was used here for crystal bending simulations. The model was tested against literature data of bending of crystal silicon [15], and then applied to cuboid crystals of high aspect ratio, fixed at the bottom face (see Fig. 9),

### 3. Results and discussion

In this study, 52 crystals were broken. More than 50% of the crystals were found to break close to the fixed point (within a distance equal to 10% of their length). The crystals tend to break some distance from the support and the glue, which indicates that the gluing process has not affected the strength of the crystals. Simulation of the crystal bending stress across a line boundary at the top of the beam (see Fig. 9) was found to reach its maximum value at 8% of the distance between the edge of the support and the location where the force is applied.

The descriptive statistics of the obtained breakage strength and Young's Modulus values are summarised in Table I (Appendix Table A.1 gives the values for each crystal). The distribution of Young's modulus values is fitted into a Weibull model and the modelled median equals 1.90 GPa, which compares well to the Young's modulus predicted for organic molecules [24]. Namazu et al. use a three point bending test on Si beams using AFM to apply the force, and found a consistent value for the Young's Modulus across different size beams (169.9 GPa, inorganic materials have typically much higher Young's modulus than organic crystals). Taylor et al. [11] observed a standard deviation of 14% in the Young's modulus from nano-indentation for pharmaceutical materials. Our study finds the Young's modulus varies randomly from crystal to crystal with a wide variation of 85% (0.163 and 12.4 GPa. Figure 10). Comparing the data from different AFM tips shows that different crystals behave differently on the same tip, and the crystal to crystal variation appears randomly spread over the tips, eliminating tip fatigue or tip to tip performance variations as a cause of the distribution (Figure 11). The quality of the glue joint that fixes the crystal on the support is a second cause of variability. Elasticity measurements on crystals in runs where crystals were bent and then returned to the rest position showed the spring

constant and thus the Young's modulus varied less than 10% (10 tests on the same crystal with increasing extend of bending). This is indicative of a good joint, but does not exclude the fact that the observed elasticity could be the result of the combined glue and crystal elasticity. However, it is interesting that Roberts et al. [6] observed the average crack length to be of the same order of magnitude as our crystals (table A.II), indicating that our assumption that a crystal is a solid beam consisting of a single continuous lattice with few faults may not be correct. The presence of defects of a size equivalent to the crystal width and height, would result in significant deviation from the ideal cantilever assumptions. In addition, it is worth noting that Matoy et al [25] using silicon oxide, oxinitride and nitride beams observed the analytical solution (eq 7) to underestimate the Young's modulus by 30%, because additional shear stresses in short and thick cantilevers, and a systematic error of the length of the cantilever beams, which has a cubic influence on the Young's modulus (eq. 7).

In any case, for each crystal the spring constant  $k_c$  remains constant during the experiment, and thus allows accurate estimation of the force. The calculated breakage force (eq 8) is thus not impacted by "give" in the glue, or unexpected changes in E from crystal to crystal due to lattice defects. The observed breakage strength also varies strongly, between 5.27 MPa and 81.1 MPa, This is however more in line with expected behaviour as it's well known that the breakage property is not just a physical material property, but rather dependent on cracks in the surface and crystal lattice that vary from crystal to crystal [26-28]. The position of crystal imperfections is critical; a small crack in the region of maximal stress could initiate the breakage process, reducing the breakage strength of the crystal with respect to another crystal with fewer defects in the high stress zone.

Tensile strength distributions are usually captured with the Weibull probability distribution function:

$$f(x, k, \lambda) = 1 - e^{-\left(\frac{x}{\lambda}\right)^k} \quad (9)$$

where  $k$  and  $\lambda$  are the Weibull repartition function shape and scale parameters respectively, and  $x$  corresponds to the distributed property values. Such distribution is more suitable for mechanical properties data than the Normal distribution [29, 30]. The utility of a distribution lies in its direct implementation in numerical investigations, e.g. Discrete Element Method (DEM), to help predict breakage due to forces applied on crystals in processing equipment [31-34].

The Weibull repartition function was fitted to the cumulative distribution values obtained by evenly distributing the logarithmic values of breakage strength and Young's modulus over 8 and 9 bins respectively (see Tables II and III, and Figure 10). The estimated Weibull parameters along with the Weibull average and median values of both distributions are tabulated in Table IV, and show 50% of the crystals experience breakage at 22.4MPa which is in good agreement with estimates of the glutamic acid breakage strength by MacLeod and Muller, who found that for 300 – 600  $\mu m$  long beta glutamic acid crystals  $\sigma_b$  was 13-17 MPa [1].

In order to gain a better understanding of the significance of each crystal dimension on the distribution of the mechanical property estimates, the monotonicity between these variables was assessed using the Spearman correlation, a rank-based statistical analysis method, which is ideal for small samples and is insensitive to extreme values.

The results of the Spearman analysis, using interval of confidence of 95% and a significance level, of 0.05, are tabulated in Table V. The coefficient of correlation takes a value between -1 (for a strictly inverse proportionality) and +1 (for a strictly positive

proportionality). A coefficient of 0 shows a non-monotonic relationship between the variables [35]. The correlation coefficient between the Young's modulus and the breakage strength is 0.544 for with a P-value well below the significance level ( $p_{corr} = 3.07 \times 10^{-5}$ ) and thus, the *stronger the crystal is, the higher the Young's modulus*. The Spearman coefficient was found equal to -0.419 with a P-value of  $2.01 \times 10^{-3}$  between crystal height and breakage strength, and -0.290 with a P-value of  $3.70 \times 10^{-2}$  for Young's Modulus. Thus, the thicker crystals deem to have a lower breakage strength (and Young's modulus). This is consistent with eq(1) if the crack length is proportional to the height of the crystals:

$$\frac{E}{\sigma_b^2 h} = 0.04 \text{ to } 0.26 \sim \frac{1}{J_{ic}} \frac{\lambda}{h} \quad (10)$$

For the data set measured, eq (10) is 10% on average, but in a wide range of 0.04 to 0.26, suggesting that the carefully crystallised crystals (seeded cooling crystallisation) have a wide range of initial crack lengths.

## 4. Conclusions

An innovative method to measure breakage strength and elastic modulus from single crystal cantilevers using Atomic Force Microscopy is presented in this study. Crystals break at ~10% of the distance between where forces in applied and the edge the cantilever hangs over, in line with prediction of 8% for linear elastic materials.

The Euler-Bernoulli beam theory was used to calculate the breakage strength and Young's modulus of 52  $\beta$ -LGA crystals. The mechanical properties data were fitted into a Weibull distribution model which defines that 50% of the crystals break at

22.4MPa and have Young's modulus below 1.90GPa. Spearman analysis demonstrated that (i) stronger crystals have a higher Young's modulus, and (ii) thicker crystals have lower breakage stress and Young's modulus, which corresponds with the established fracture mechanics theory.

The data generated using the single crystal cantilever method provides the fundamental material properties essential for understanding of undesirable crystal fracture in manufacturing processes such as crystallisation, filtration and drying of chemical ingredients but the broad range of  $E$  and  $\sigma_b$  values reported suggests a significant extend of crystal imperfections, even though the crystals where carefully crystallised using a seeded cooling crystallisation.

## **5. Acknowledgements**

We would like to thank Satpal Sohi for providing insights in the sample preparation. The support of the EPSRC Centre for Doctoral Training in Complex Particulate Products and Processes (CDT CP3) is gratefully acknowledged. ISF also acknowledges the support of the Advanced Manufacturing Supply Chain Initiative through the funding of the Advanced Digital Design of Pharmaceutical Therapeutics (ADDoPT) project (Grant No. 14060).

## 6. References

- [1] C.S. MacLeod, F.L. Muller, On the fracture of pharmaceutical needle-shaped crystals during pressure filtration: case studies and mechanistic understanding, *Organic Process Research & Development* 16 (2012) 425-434.
- [2] E. Kougioulos, C. Chadwick, M. Ticehurst, Impact of agitated drying on the powder properties of an active pharmaceutical ingredient, *Powder technology* 210 (2011) 308-314.
- [3] N. Sandler, D. Wilson, Prediction of granule packing and flow behavior based on particle size and shape analysis, *Journal of pharmaceutical sciences* 99 (2010) 958-968.
- [4] X.Y. Lawrence, Pharmaceutical quality by design: product and process development, understanding, and control, *Pharmaceutical research* 25 (2008) 781-791.
- [5] F.L. Muller, On the rheological behaviour of batch crystallisations, *Chemical Engineering Research and Design* 87 (2009) 627-632.
- [6] R. Roberts, R. Rowe, P. York, The relationship between the fracture properties, tensile strength and critical stress intensity factor of organic solids and their molecular structure, *International journal of pharmaceutics* 125 (1995) 157-162.
- [7] R.J. Roberts, R.C. Rowe, P. York, The relationship between Young's modulus of elasticity of organic solids and their molecular structure, *Powder Technology* 65 (1991) 139-146.
- [8] C.C. Kwan, Y.Q. Chen, Y.L. Ding, D.G. Papadopoulos, A.C. Bentham, M. Ghadiri, Development of a novel approach towards predicting the milling behaviour of pharmaceutical powders, *European Journal of Pharmaceutical Sciences* 23 (2004) 327-336.
- [9] J. Ast, M. Ghidelli, K. Durst, M. Göken, M. Sebastiani, A.M. Korsunsky, A review of experimental approaches to fracture toughness evaluation at the micro-scale, *Materials & Design* 173 (2019) 107762.
- [10] K. Ramos, D. Bahr, Mechanical behavior assessment of sucrose using nanoindentation, *Journal of materials research* 22 (2007) 2037-2045.
- [11] L. Taylor, D. Papadopoulos, P. Dunn, A. Bentham, N. Dawson, J. Mitchell, M. Snowden, Predictive milling of pharmaceutical materials using nanoindentation of single crystals, *Organic Process Research & Development* 8 (2004) 674-679.
- [12] H.-J. Butt, B. Cappella, M. Kappl, Force measurements with the atomic force microscope: Technique, interpretation and applications, *Surface science reports* 59 (2005) 1-152.

- [13] B. Du, O.K. Tsui, Q. Zhang, T. He, Study of elastic modulus and yield strength of polymer thin films using atomic force microscopy, *Langmuir* 17 (2001) 3286-3291.
- [14] V.M. Masterson, X. Cao, Evaluating particle hardness of pharmaceutical solids using AFM nanoindentation, *International journal of pharmaceutics* 362 (2008) 163-171.
- [15] T. Namazu, Y. Isono, T. Tanaka, Evaluation of size effect on mechanical properties of single crystal silicon by nanoscale bending test using AFM, *Journal of Microelectromechanical Systems* 9 (2000) 450-459.
- [16] S. Ghosh, M.K. Mishra, S.B. Kadambi, U. Ramamurty, G.R. Desiraju, Designing Elastic Organic Crystals: Highly Flexible Polyhalogenated N-Benzylideneanilines, *Angewandte Chemie International Edition* 54 (2015) 2674-2678.
- [17] A.P. Shier, *The Breakage of Needle-Shaped Crystals Under Pressure Filtration*, University of Leeds, 2017.
- [18] M.J. O'Neil, *The Merck index: an encyclopedia of chemicals, drugs, and biologicals*, RSC Publishing 2013.
- [19] V.A. Pertzoff, The solubility of glutamic acid in water and certain organic solvents, *Journal of Biological Chemistry* 100 (1933) 97-104.
- [20] S.J. Grutzik, R.S. Gates, Y.B. Gerbig, D.T. Smith, R.F. Cook, A.T. Zehnder, Accurate spring constant calibration for very stiff atomic force microscopy cantilevers, *Review of Scientific Instruments* 84 (2013) 113706.
- [21] R. Hooke, 1678, *De Potentia Restitutiva, or of Spring, Explaining the Power of Springing Bodies* (London: J. Martyn) (2007).
- [22] M.R. Lindeburg, *Mechanical engineering reference manual for the PE exam*, www.ppi2pass.com 2013.
- [23] S. Timoshenko, *History of strength of materials: with a brief account of the history of theory of elasticity and theory of structures*, Courier Corporation 1983.
- [24] G.M. Day, S.L. Price, M. Leslie, Elastic constant calculations for molecular organic crystals, *Crystal Growth & Design* 1 (2001) 13-27.
- [25] K. Matoy, H. Schönherr, T. Detzel, T. Schöberl, R. Pippan, C. Motz, G. Dehm, A comparative micro-cantilever study of the mechanical behavior of silicon based passivation films, *Thin Solid Films* 518 (2009) 247-256.
- [26] M. Descamps, *Disordered pharmaceutical materials*, John Wiley & Sons 2016.
- [27] J.N. Sherwood, Fifty years as a crystal gazer: life as an imperfectionist, *Crystal growth & design* 4 (2004) 863-877.
- [28] C. Fuller, The Chemistry of Imperfect Crystals, *Journal of the American Chemical Society* 86 (1964) 4514-4515.

- [29] W. Weibull, Wide applicability, *Journal of applied mechanics* 103 (1951) 293-297.
- [30] L. Vogel, W. Peukert, Breakage behaviour of different materials—construction of a mastercurve for the breakage probability, *Powder Technology* 129 (2003) 101-110.
- [31] Z. Grof, M. Kohout, F. Štěpánek, Multi-scale simulation of needle-shaped particle breakage under uniaxial compaction, *Chemical Engineering Science* 62 (2007) 1418-1429.
- [32] Z. Grof, C.M. Schoellhammer, P. Rajniak, F. Štěpánek, Computational and experimental investigation of needle-shaped crystal breakage, *International journal of pharmaceutics* 407 (2011) 12-20.
- [33] K. Sato, H. Nagai, K. Hasegawa, K. Tomori, H. Kramer, P. Jansens, Two-dimensional population balance model with breakage of high aspect ratio crystals for batch crystallization, *Chemical Engineering Science* 63 (2008) 3271-3278.
- [34] D.J. Lamberto, B. Cohen, J. Marencic, C. Miranda, R. Petrova, L. Sierra, Laboratory methods for assessing API sensitivity to mechanical stress during agitated drying, *Chemical engineering science* 66 (2011) 3868-3875.
- [35] G. Saporta, *Probabilités, analyse des données et statistique*, Editions Technip2006.

## 7. List of figures

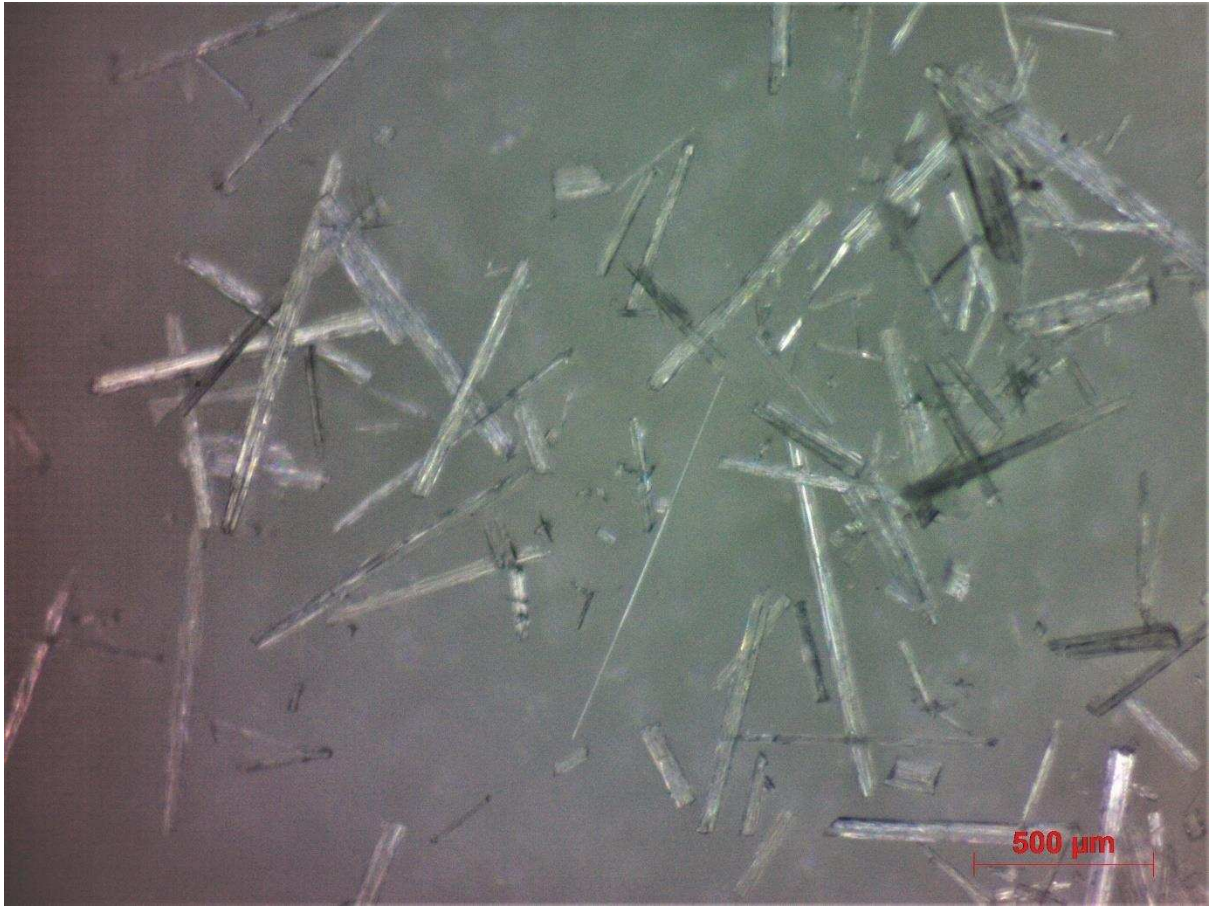


Figure 1: Light microscope image of the re-crystallised  $\beta$ -LGA crystals.

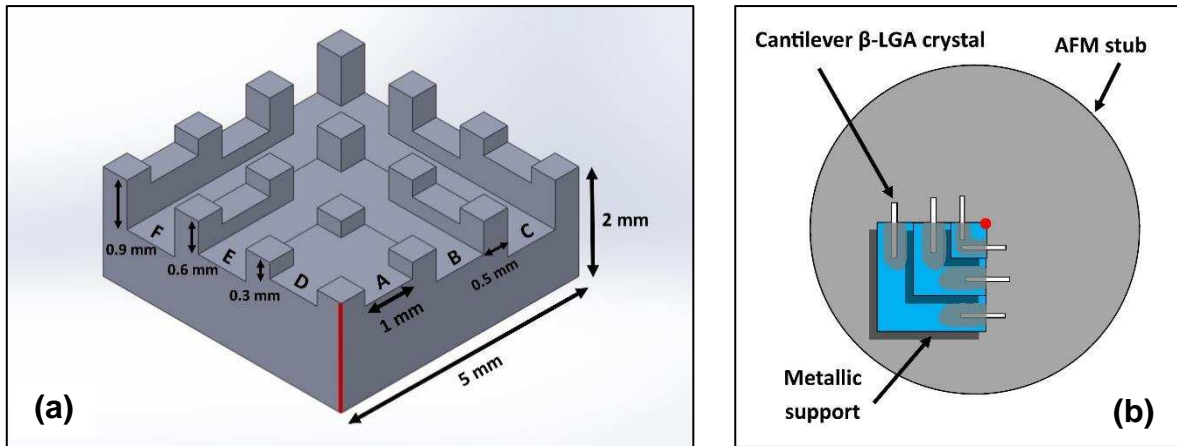


Figure 2: Schematic of (a) the metallic support (6 crystals can be mounted as cantilevers on positions A to F) and (b) the AFM magnetic stub (the corner of the metallic support highlighted in red is positioned at the centre of the AFM stub).

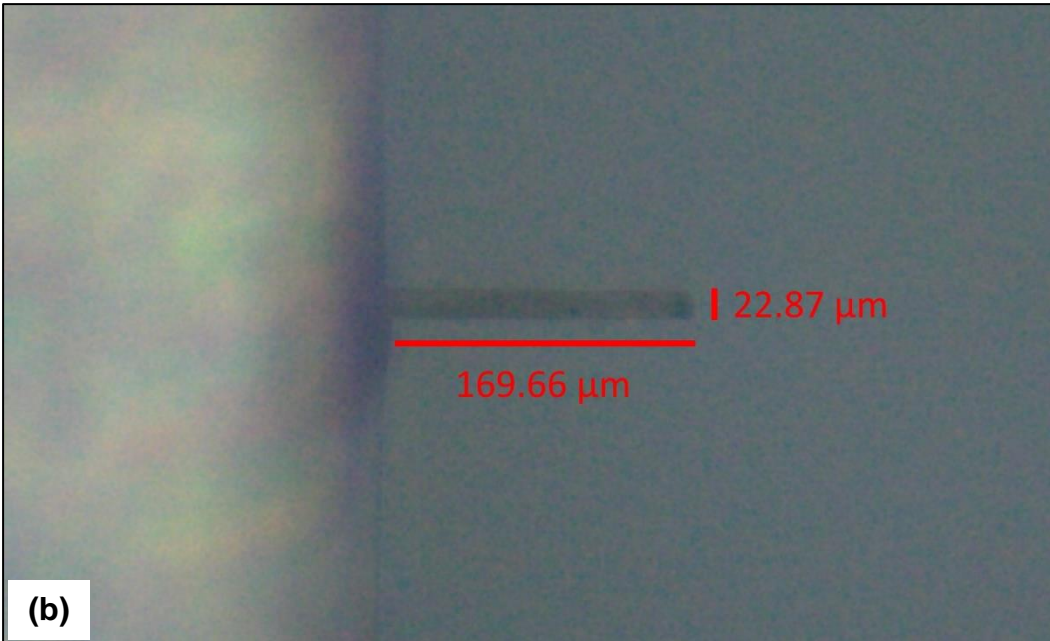
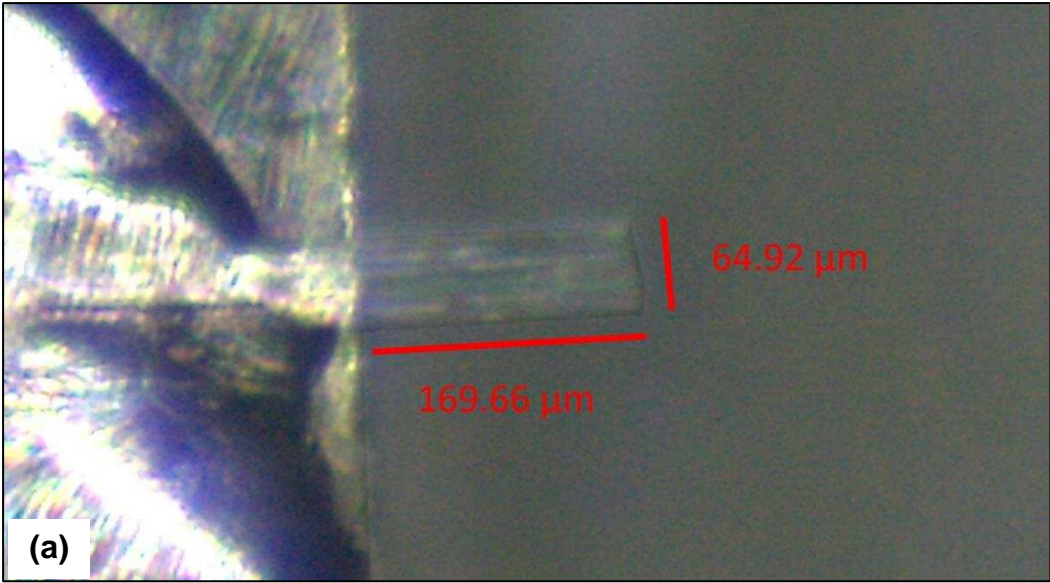


Figure 3: (a) Top and (b) lateral views of a mounted crystal (see No38 in Table A.1).  
The image was produced using a light microscope at x5 magnification.

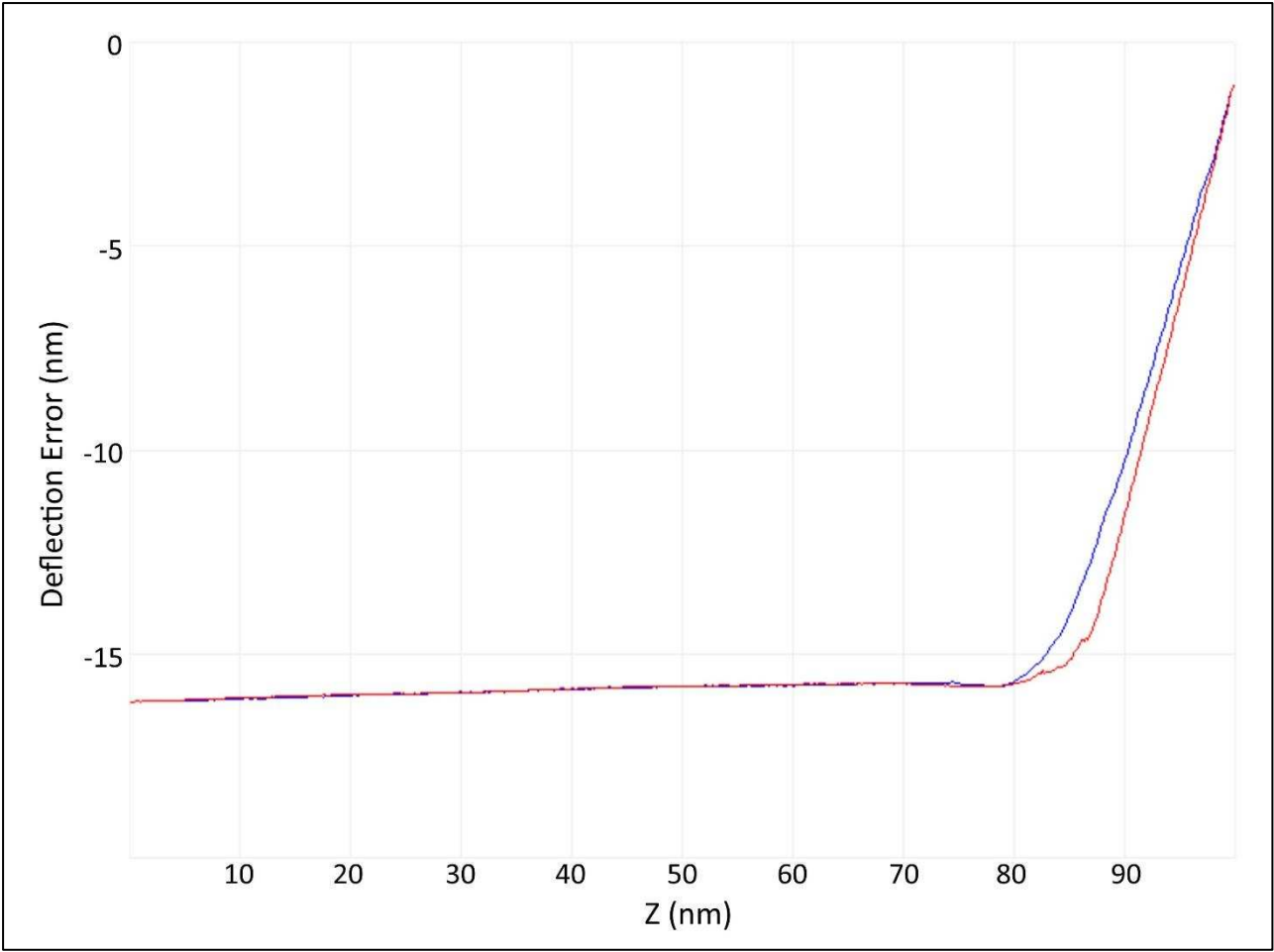


Figure 4: Ramp curve on Bruker Sapphire-12M used for the AFM probe calibration.

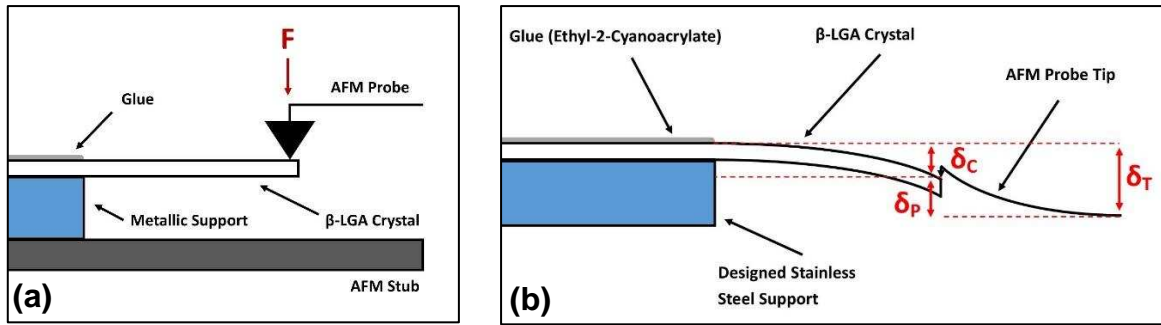


Figure 5: Schematic representation of (a) the force application on the  $\beta$ -LGA cantilever and (b) the AFM probe and  $\beta$ -LGA cantilever deflections.

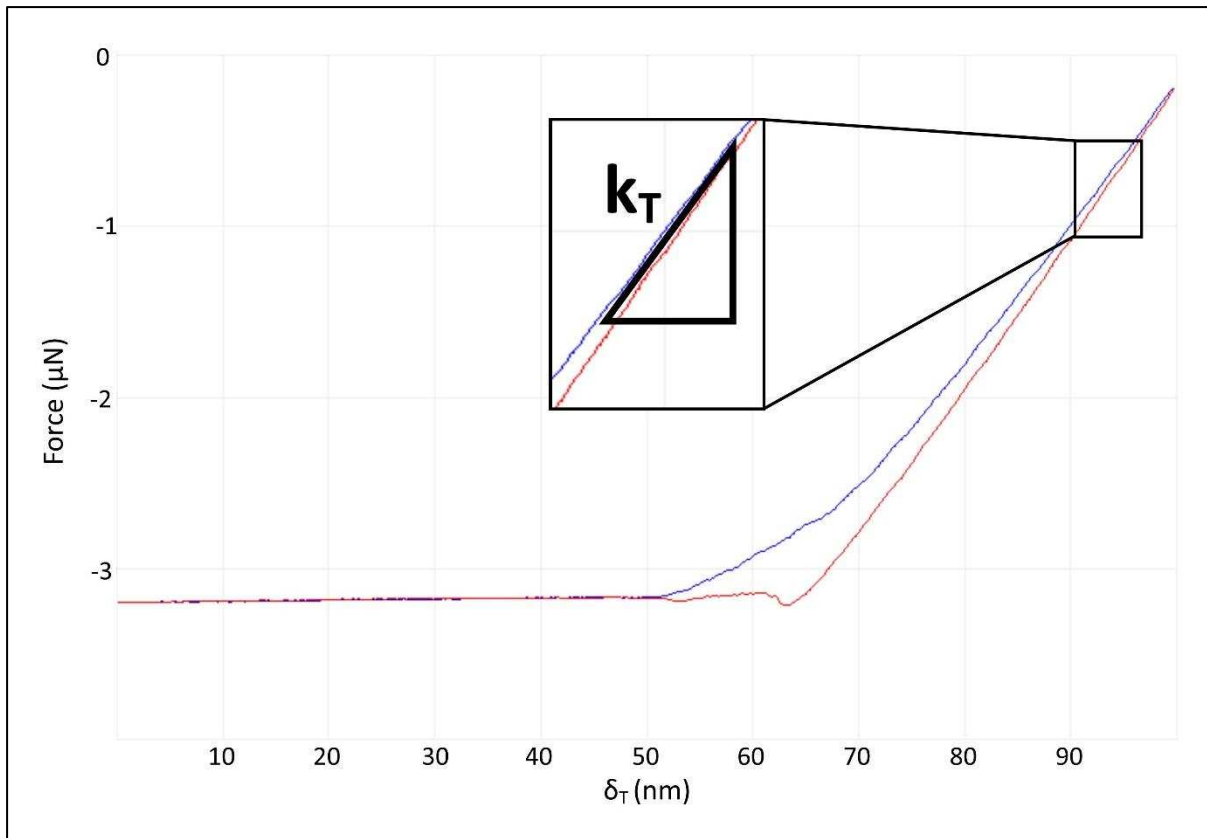


Figure 6: Ramp loading (blue)/unloading (red) curve of a Bruker RTESP-525 AFM probe engaged on the beta-LGA cantilever. The system spring,  $k_T$ , is equal to the gradient of the loading/unloading curve ( $k_T = \text{Force}/\delta_T$ ).

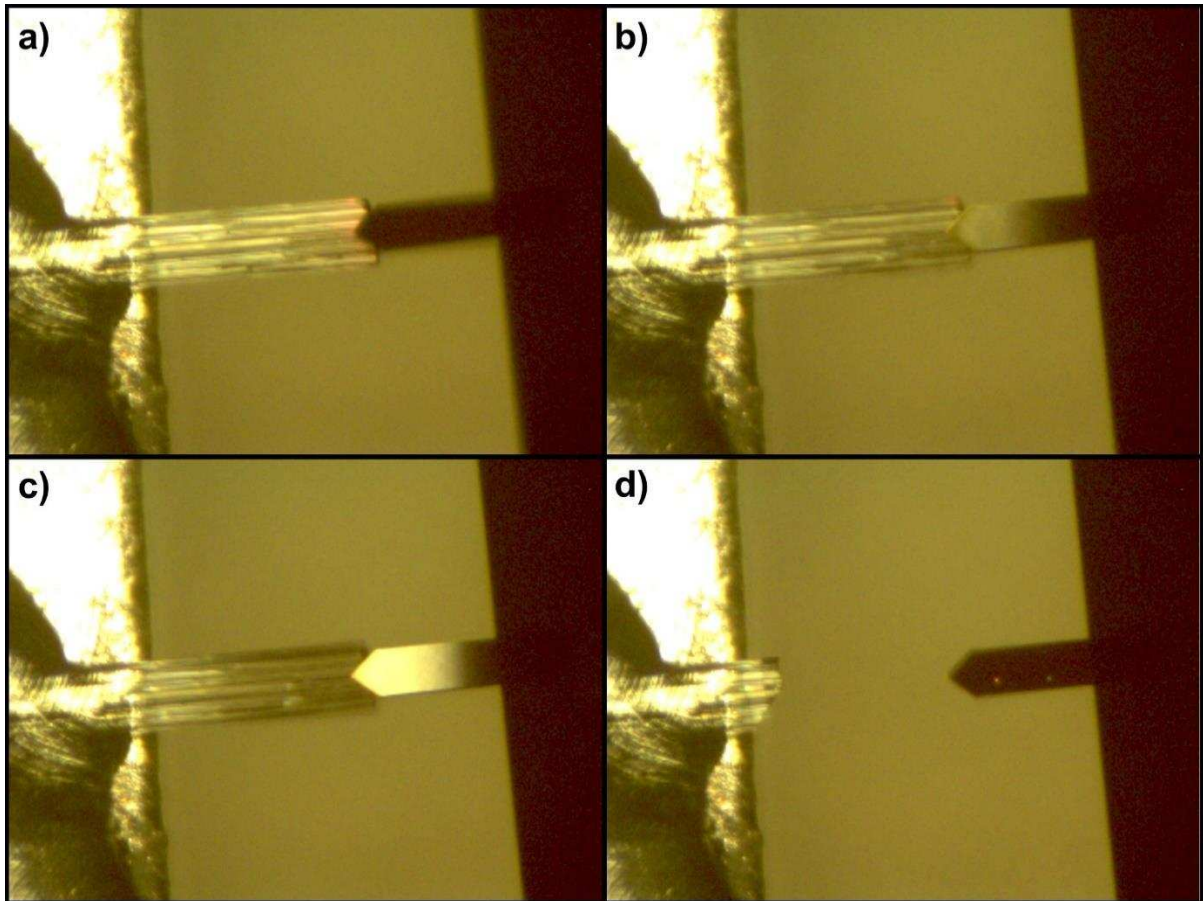


Figure 7: Top view of the AFM probe engagement at the tip of the glued crystal at different step motor deflections: a) 0 steps, b) 40 steps, c) 60 steps and d) 63 steps (when crystal breakage was occurred).

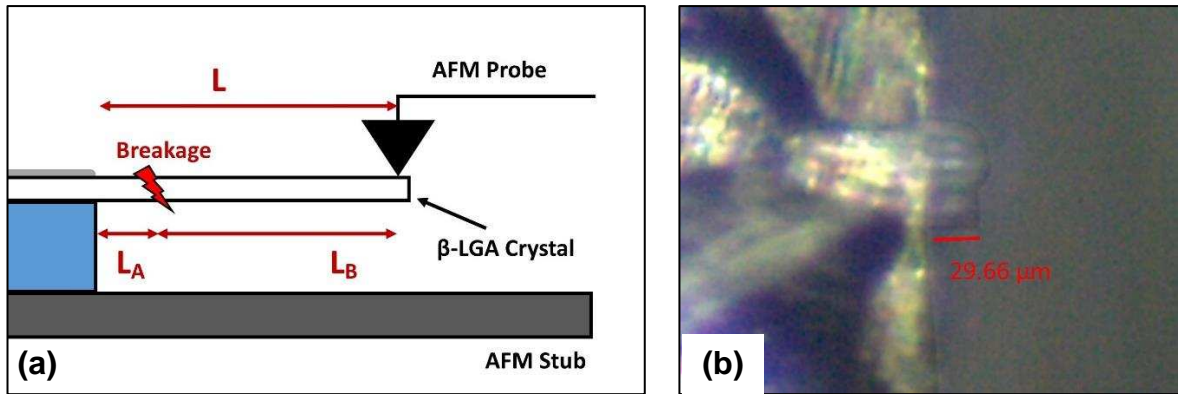


Figure 8: (a) Schematic representation of the crystal length before and after breakage and (b) top view of the crystal after breakage. The image was produced using a light microscope at x5 magnification.



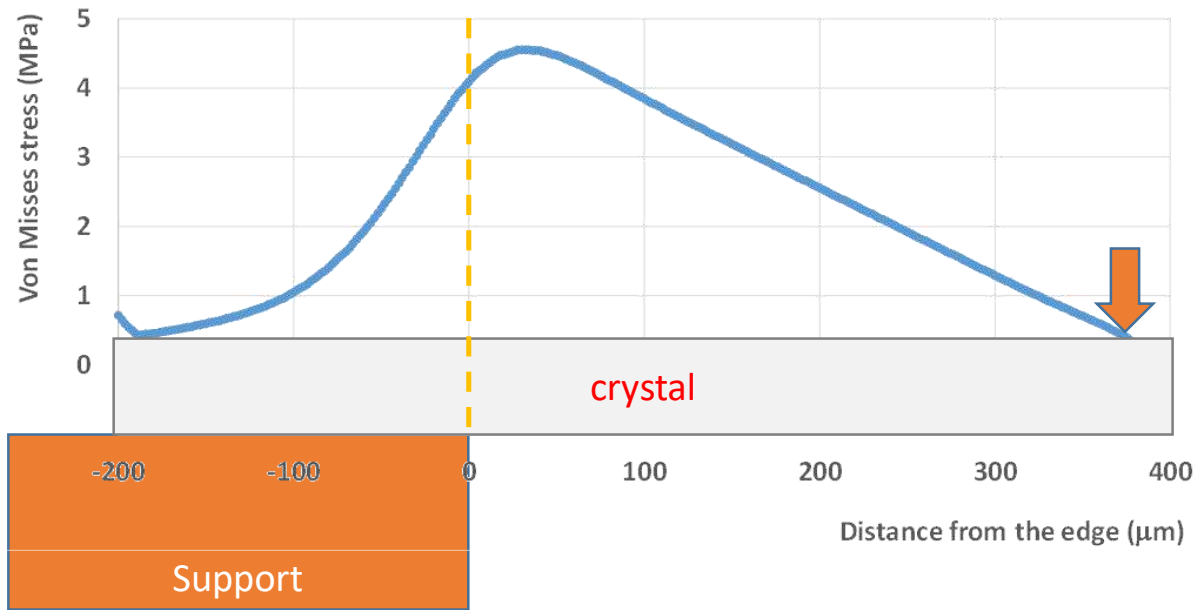


Figure 9: Predicted von Mises stress along the crystal arc length. The crystal is fixed on a support and the force applied  $\sim 375 \mu\text{m}$  from the edge of the support.

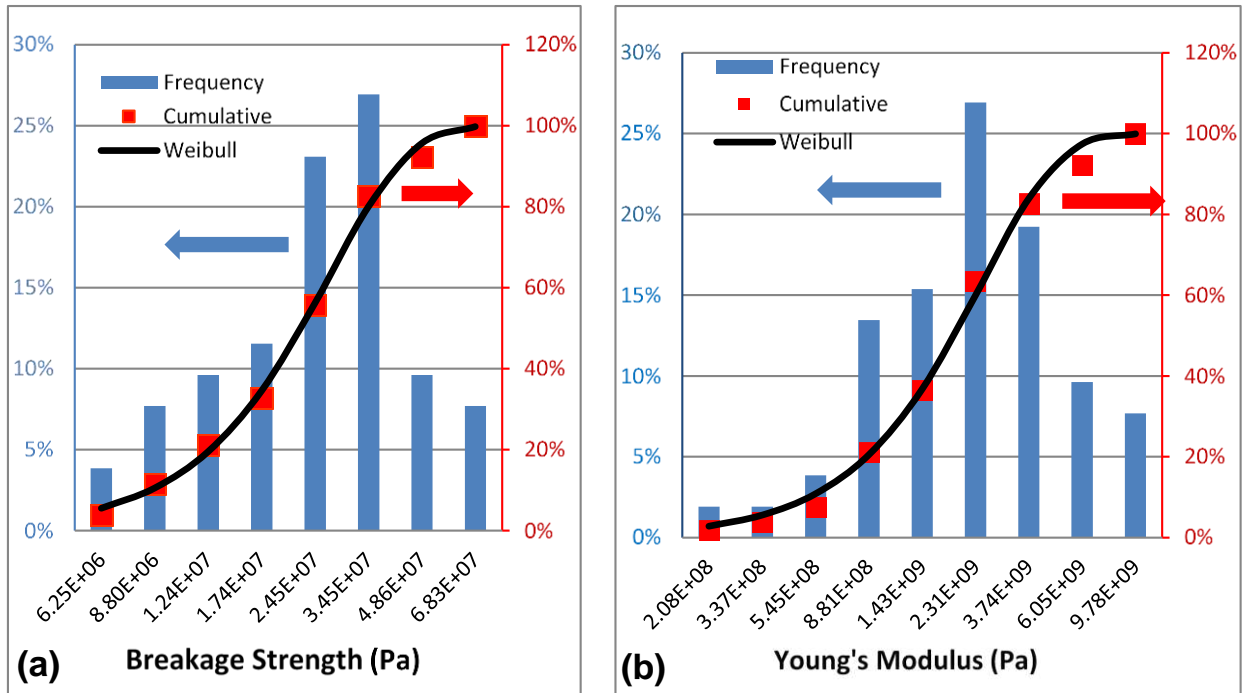


Figure 10: Distribution of (a) breakage strength (individual data can be found in Table II) and (b) Young's Modulus (individual data can be found in Table III).

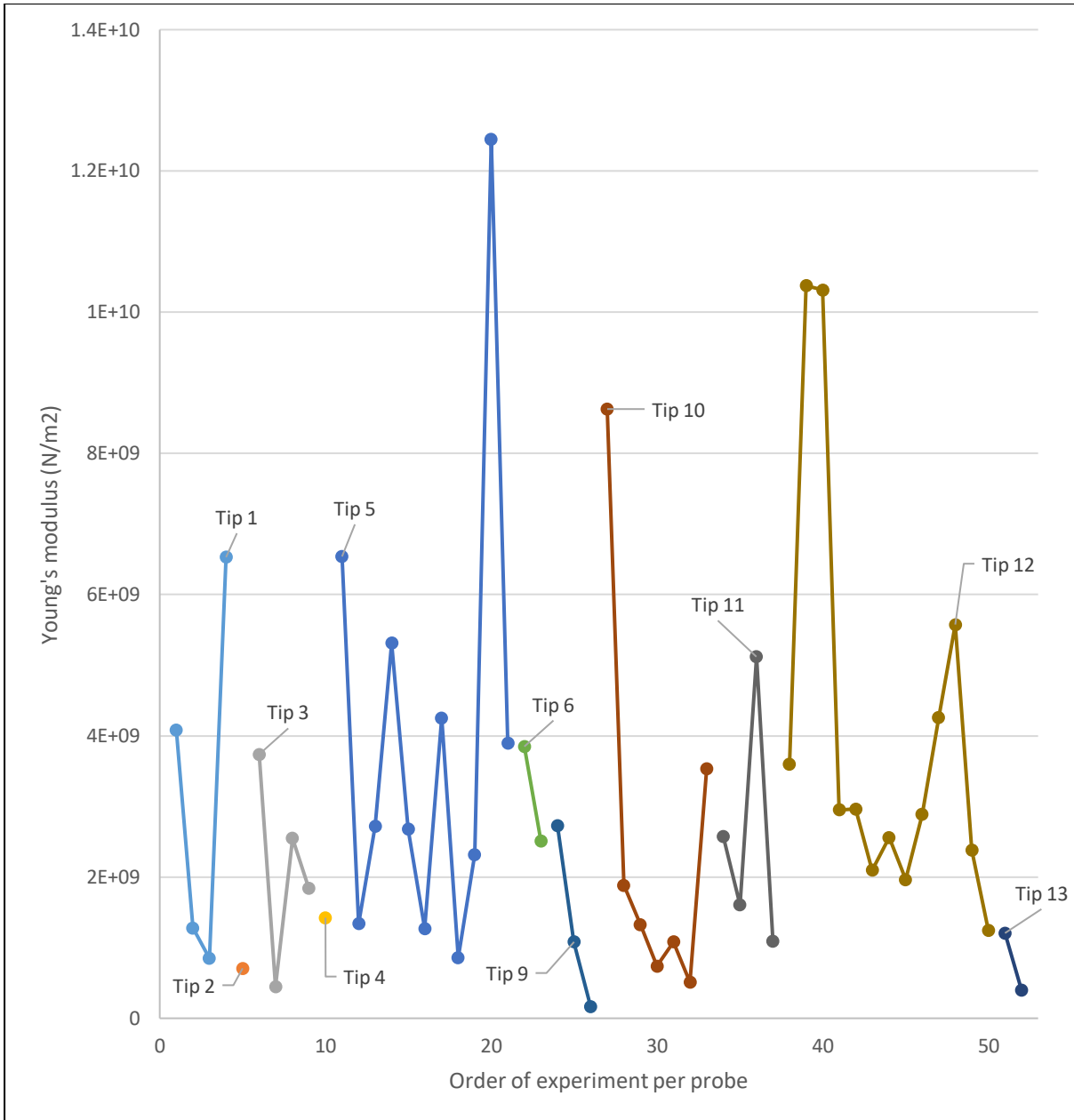


Figure 11: Crystals Young's Modulus values against the associated probe and order of usage (individual data can be found in Table A.I).

## 8. List of tables

Table I: Descriptive statistical analysis data for the sample of 52 crystal breakage experiments.

	Minimum	Maximum	Average	Standard Deviation
L, crystal length (m)	1.02E-04	6.07E-04	2.52E-04	1.14E-04
L <sub>B</sub> , crystal broken length (m)	8.66E-05	5.33E-04	2.11E-04	9.53E-05
w, width (m)	2.59E-05	9.59E-05	6.27E-05	1.59E-05
h, height (m)	1.40E-05	6.36E-05	3.49E-05	9.32E-06
F <sub>B</sub> , breakage force (N)	2.83E-04	6.35E-03	1.84E-03	1.31E-03
σ <sub>B</sub> , breakage strength (Pa)	5.27E+06	8.11E+07	2.92E+07	1.58E+07
E, Young's modulus (Pa)	1.63E+08	1.24E+10	3.08E+09	2.64E+09

Table II: Breakage strength distribution data.

Bin Index	Bin Average Value (Pa)	Bin Average Value (Log)	$N_{br}$	Frequency	Cumulative $N_{br}$	%Cumul	Weibull %Cumul
1	6.25E+06	6.80	2	3.8%	2	3.8%	5.57%
2	8.80E+06	6.94	4	7.7%	6	11.5%	10.57%
3	1.24E+07	7.09	5	9.6%	11	21.2%	19.56%
4	1.74E+07	7.24	6	11.5%	17	32.7%	34.56%
5	2.45E+07	7.39	12	23.1%	29	55.8%	56.24%
6	3.45E+07	7.54	14	26.9%	43	82.7%	80.02%
7	4.86E+07	7.69	5	9.6%	48	92.3%	95.66%
8	6.83E+07	7.83	4	7.7%	52	100%	99.78%

Table III: Young's modulus distribution data.

Bin Index	Bin Average Value (Pa)	Bin Average Value (Log)	$N_{br}$	Frequency	Cumulative $N_{br}$	%Cumul	Weibull %Cumul
1	2.08E+08	8.32	1	1.9%	1	1.9%	2.84%
2	3.37E+08	8.53	1	1.9%	2	3.8%	5.60%
3	5.45E+08	8.74	2	3.8%	4	7.7%	10.87%
4	8.81E+08	8.95	7	13.5%	11	21.2%	20.53%
5	1.43E+09	9.15	8	15.4%	19	36.5%	36.80%
6	2.31E+09	9.36	14	26.9%	33	63.5%	60.00%
7	3.74E+09	9.57	10	19.2%	43	82.7%	83.96%
8	6.05E+09	9.78	5	9.6%	48	92.3%	97.41%
9	9.78E+09	9.99	4	7.7%	52	100.0%	99.93%

Table IV: Weibull distribution parameters.

Weibull	Breakage Strength, $\sigma_B$	Young's Modulus, E
Nbr of Bins	8	9
Shape parameter k	1.95274	1.43674
Scale parameter $\lambda$	2.70E+07	2.45E+09
Median	2.24E+07	1.90E+09
Average	2.40E+07	2.23E+09
R <sup>2</sup>	0.99670	0.99509

Table V: Spearman correlation analysis. The shaded columns have P-values larger than the significance limit of 0.05

Spearman Correlation (N=52, $\alpha=0.05$ )		$L_B$ , crystal broken length	L, crystal length	w, width	h, height	$\sigma_B$ , breakage strength
$\sigma_B$ , breakage strength	Corr.	0.259	0.131	0.0444	<b>-0.419</b>	-
	P-value	0.0637	0.356	0.755	<b>0.00201</b>	-
E, Young's modulus	Corr.	0.215	0.254	0.206	<b>-0.290</b>	<b>0.544</b>
	P-value	0.126	0.0691	0.142	<b>0.0370</b>	<b>3.07E-05</b>

## 9. APPENDIX

### A.1. Derivation of Equation (2)

Using Hooke's law (see Eq. 1) to calculate the spring constant and dividing the spring constant of the crystal by the spring constant of the probe gives:

$$\frac{k_C}{k_P} = \frac{F/\delta_C}{F/\delta_P} \quad (\text{A1})$$

Re-arranging Eq. A1 gives:

$$k_C = k_P \cdot \frac{\delta_P}{\delta_C} \quad (\text{A2})$$

Taking into account that the total displacement is equal to the sum of the crystal and the probe displacements,  $\delta_T = \delta_C + \delta_P$  (see Figure 5b), Eq. A2 takes the following form:

$$k_C = k_P \cdot \frac{\delta_P}{(\delta_T - \delta_P)} \quad (\text{A3})$$

Multiplying and dividing by  $\delta_T$  gives:

$$k_C = \frac{k_P}{\delta_T} \cdot \frac{\delta_T \cdot \delta_P}{(\delta_T - \delta_P)} \quad (\text{A4})$$

Re-arranging Eq. A4:

$$k_C = \frac{k_P / \delta_T}{\frac{1}{\delta_P} - \frac{1}{\delta_T}} \quad (\text{A5})$$

Multiplying and dividing by F gives:

$$k_C = \frac{k_P \cdot \frac{F}{\delta_T}}{\frac{F}{\delta_P} - \frac{F}{\delta_T}} \quad (\text{A6})$$

Taking into account Hooke's law results:

$$k_C = \frac{d k_P}{(1-d)} \rightarrow k_P = \left(\frac{1}{d} - 1\right) k_C \quad (\text{A7})$$

## A.2 Derivation of Equation (3)

Multiplying both sides of  $\delta_T = \delta_C + \delta_P$  by  $\delta_C$  and re-arranging gives:

$$\delta_C = \frac{\delta_T \delta_C}{\delta_C + \delta_P} \quad (\text{A8})$$

Dividing the numerator and the denominator of the right hand side by F gives:

$$\delta_C = \delta_T \cdot \frac{\delta_C / F}{\frac{\delta_C}{F} + \frac{\delta_P}{F}} \quad (\text{A9})$$

Taking into account Hooke's law results:

$$\delta_C = \delta_T \cdot \frac{1/k_C}{\frac{1}{k_C} + \frac{1}{k_P}} \quad (\text{A10})$$

Re-arranging Eq. A10 gives:

$$\delta_C = \delta_T \cdot \frac{k_P}{k_P + k_C} \quad (\text{A11})$$

Table A.I: Experimental data and calculated mechanical properties for 52 crystals.

Crystal No	Probe No	L, crystal length (m)	w, width (m)	h, height (m)	$k_T$ , crystal/probe system spring (N/m)	E, Young's modulus (Pa)	$n_{steps}$ , motor steps	$L_B$ , crystal broken length (m)	$F_B$ , breakage force (N)	$\sigma_B$ , breakage strength (Pa)
1	1	1.71E-04	6.10E-05	1.40E-05	29.43	4.08E+09	54	1.40E-04	7.41E-04	5.18E+07
2	2	1.59E-04	8.67E-05	2.95E-05	65.63	7.07E+08	104	9.97E-05	3.18E-03	2.52E+07
3	1	2.04E-04	5.34E-05	2.95E-05	40.90	1.28E+09	56	1.87E-04	1.07E-03	2.59E+07
4	1	3.71E-04	6.76E-05	4.39E-05	21.15	8.48E+08	107	1.99E-04	1.05E-03	9.69E+06
5	1	4.85E-04	5.97E-05	3.89E-05	40.04	6.53E+09	137	4.03E-04	2.56E-03	6.86E+07
6	3	2.50E-04	6.37E-05	3.59E-05	93.63	3.74E+09	45	2.50E-04	1.96E-03	3.59E+07
7	3	1.02E-04	3.94E-05	3.69E-05	102.22	4.50E+08	69	9.37E-05	3.29E-03	3.45E+07
8	3	6.07E-04	7.66E-05	5.60E-05	32.18	2.55E+09	71	3.56E-04	1.06E-03	9.45E+06
9	3	3.94E-04	7.64E-05	4.07E-05	32.57	1.84E+09	110	3.18E-04	1.67E-03	2.51E+07
10	4	2.44E-04	7.21E-05	3.84E-05	66.47	1.42E+09	75	2.19E-04	2.32E-03	2.88E+07
11	5	1.53E-04	8.29E-05	4.07E-05	168.18	2.72E+09	57	1.21E-04	4.47E-03	2.37E+07
12	5	1.92E-04	7.05E-05	2.80E-05	118.14	5.31E+09	37	1.58E-04	2.04E-03	3.50E+07
13	5	1.45E-04	6.94E-05	2.29E-05	63.12	1.34E+09	33	1.20E-04	9.71E-04	1.92E+07
14	5	2.88E-04	4.72E-05	2.30E-05	32.77	6.54E+09	43	2.23E-04	6.57E-04	3.52E+07

15	5	2.87E-04	5.98E-05	2.54E-05	33.71	3.90E+09	40	2.21E-04	6.28E-04	2.15E+07
16	5	1.48E-04	8.26E-05	2.80E-05	179.23	1.24E+10	76	1.38E-04	6.35E-03	8.11E+07
17	5	1.44E-04	6.74E-05	2.87E-05	121.77	2.32E+09	24	1.39E-04	1.36E-03	2.05E+07
18	5	2.69E-04	4.50E-05	2.70E-05	38.66	4.25E+09	37	2.08E-04	6.67E-04	2.54E+07
19	5	1.14E-04	8.57E-05	4.46E-05	169.34	8.57E+08	68	1.07E-04	5.37E-03	2.01E+07
20	5	2.71E-04	5.93E-05	3.59E-05	63.57	2.68E+09	46	1.61E-04	1.36E-03	1.72E+07
21	5	1.84E-04	7.04E-05	4.20E-05	114.26	1.27E+09	43	1.32E-04	2.29E-03	1.46E+07
22	6	1.73E-04	7.16E-05	3.69E-05	136.72	2.51E+09	46	1.73E-04	2.93E-03	3.13E+07
23	6	2.34E-04	7.31E-05	2.44E-05	57.38	3.85E+09	46	2.16E-04	1.23E-03	3.65E+07
24	9	1.70E-04	5.97E-05	1.91E-05	45.01	2.73E+09	27	1.70E-04	5.66E-04	2.65E+07
25	9	2.73E-04	7.63E-05	3.69E-05	40.72	1.08E+09	47	2.73E-04	8.92E-04	1.40E+07
26	9	1.59E-04	3.28E-05	6.04E-05	53.70	1.63E+08	34	1.23E-04	8.51E-04	5.27E+06
27	10	3.31E-04	7.12E-05	3.69E-05	102.98	8.63E+09	64	2.43E-04	3.07E-03	4.63E+07
28	10	3.29E-04	4.32E-05	3.05E-05	15.05	1.88E+09	140	3.00E-04	9.82E-04	4.39E+07
29	10	1.82E-04	3.30E-05	2.67E-05	24.84	1.08E+09	66	1.39E-04	7.64E-04	2.71E+07
30	10	3.14E-04	6.51E-05	3.71E-05	17.88	7.37E+08	80	2.86E-04	6.67E-04	1.28E+07

31	10	3.04E-04	8.32E-05	4.20E-05	53.31	1.33E+09	115	3.04E-04	2.86E-03	3.55E+07
32	10	1.73E-04	2.59E-05	4.32E-05	40.81	5.10E+08	76	1.73E-04	1.45E-03	3.11E+07
33	10	3.12E-04	6.53E-05	3.30E-05	51.05	3.53E+09	64	2.60E-04	1.52E-03	3.33E+07
34	11	2.01E-04	3.87E-05	2.93E-05	56.10	2.58E+09	24	1.77E-04	6.27E-04	2.00E+07
35	11	1.91E-04	5.19E-05	3.43E-05	75.20	1.60E+09	20	1.74E-04	7.01E-04	1.20E+07
36	11	3.67E-04	9.59E-05	4.83E-05	116.82	5.12E+09	37	1.85E-04	2.01E-03	9.99E+06
37	11	1.67E-04	7.51E-05	3.31E-05	88.18	1.09E+09	34	1.67E-04	1.40E-03	1.71E+07
38	12	1.70E-04	6.49E-05	2.29E-05	83.39	3.60E+09	63	1.40E-04	2.45E-03	6.06E+07
39	12	5.90E-04	7.84E-05	3.44E-05	33.58	1.04E+10	120	5.33E-04	1.88E-03	6.48E+07
40	12	1.79E-04	8.09E-05	3.31E-05	173.66	1.03E+10	48	1.23E-04	3.88E-03	3.24E+07
41	12	2.02E-04	5.22E-05	2.54E-05	55.80	2.95E+09	50	1.80E-04	1.30E-03	4.16E+07
42	12	1.28E-04	7.15E-05	3.19E-05	160.59	2.96E+09	49	1.28E-04	3.67E-03	3.88E+07
43	12	1.83E-04	5.21E-05	3.31E-05	89.40	2.09E+09	32	1.60E-04	1.33E-03	2.25E+07
44	12	3.65E-04	5.87E-05	3.31E-05	24.41	2.56E+09	109	3.65E-04	1.24E-03	4.24E+07
45	12	2.86E-04	4.93E-05	3.43E-05	34.65	1.96E+09	67	2.86E-04	1.08E-03	3.19E+07
46	12	4.57E-04	6.09E-05	3.82E-05	22.79	2.89E+09	120	4.20E-04	1.27E-03	3.61E+07

47	12	1.17E-04	4.47E-05	6.36E-05	196.03	5.58E+09	50	9.02E-05	4.57E-03	1.37E+07
48	12	3.86E-04	6.99E-05	3.81E-05	52.94	4.25E+09	59	3.86E-04	1.46E-03	3.31E+07
49	12	3.24E-04	8.45E-05	3.94E-05	62.34	2.38E+09	70	2.52E-04	2.03E-03	2.34E+07
50	12	2.11E-04	3.59E-05	2.84E-05	23.87	1.24E+09	62	1.99E-04	6.90E-04	2.85E+07
51	13	1.21E-04	5.21E-05	4.26E-05	106.26	3.98E+08	22	8.66E-05	1.09E-03	6.00E+06
52	13	3.14E-04	4.51E-05	3.22E-05	13.58	1.21E+09	44	2.86E-04	2.83E-04	1.04E+07

Table A.II: Literature values of mechanical properties for organic materials

Material	$E_a$ (GPa)	$\sigma_B$ (MPa)	$K_{IC}$ (MPa m <sup>0.5</sup> )	$\lambda$ ( $\mu$ m)	Method [ref]
phenylbutazone	3.33	6.8	0.14	424	PE [3][7]
ibuprofen	5.02	7.71	0.104	182	PE [3][7]
sulfadiazine	7.70	8.04	0.148	339	PE [3][7]
tolbutamide	5.22	9.6	0.113	139	PE [3][7]
caffeine (anhydrous)	8.73	9.93	0.261	691	PE [3][7]
aspirin	7.45	11.89	0.156	172	PE [3][7]
theophylline (anhydrous)	12.93	13.33	0.264	392	PE [3][7]
paracetamol		13.38	0.115	74	PE [3][7]
$\alpha$ -lactose monohydrate	24.06	18.33	0.345	354	PE [3][7]
sildenafil citrate	13.9 $\pm$ 1.5		0.02 $\pm$ 0.01		NI [11]
pharma compound c	14.9 $\pm$ 1.3		0.05 $\pm$ 0.01		NI [11]
pharma compound b	7.6 $\pm$ 0.5		0.04 $\pm$ 0.01		NI [11]
pharma compound a	2.9 $\pm$ 0.4		0.06 $\pm$ 0.00	(15-70)*	NI [11]
voriconazole	3.7 $\pm$ 0.4				NI [11]

\* range depending on applied load; PE: porosity extrapolation, NI nano indentation